Progress In Electromagnetics Research C, Vol. 103, 71–82, 2020

Improving Bandwidth, Gain and Aperture Efficiency of Patch Antenna Using Hybrid AMC Ground Plane

Jean de D. Ntawangaheza, Liguo Sun*, Yongjie Li, and Zipeng Xie

Abstract—This paper proposes a new method to enhance the impedance bandwidth (IBW), broadside gain, front-to-back ratio, and aperture efficiency of a rectangular microstrip patch antenna (RMPA) printed on a compact artificial magnetic conductor ground plane (AMC-GND). The technique uses large shorted unit cells at the center of the AMC and a wide slot cut on the unit cells located under the patch to respectively impede the propagation of surface currents and reduce the adverse effect of the loading capacitance created between the RMPA and the AMC-GND on the antenna IBW. The proposed antenna with dimensions of only $1\lambda_0 \times 0.6\lambda_0 \times 0.06\lambda_0$ realizes an IBW of 24% (6.07–7.73 GHz), peak gain of 9.93 dBi, and a simulated aperture efficiency of more than 96%. Due to its compact size, good radiation, and wide IBW performances, the presented antenna can be used in various applications, such as MIMO antenna system, wide-angle scanning antenna array, and reflector feed antennas operating in satellite C-band 5.9–6.4 GHz and 6.425–6.75 GHz. It is worth mentioning that the main contribution of the current work is the investigation of the detrimental effects of the overlay capacitor on the IBW of a linearly polarized RMPA etched on a compact AMC surface using a simple equivalent circuit model.

1. INTRODUCTION

Printed antennas, such as microstrip patch antennas (MPAs), are commonly used in many modern mobile and wireless communication systems, as they have low profile, light weight, easy fabrication, and low cost. However, classical MPAs have limited impedance bandwidth (IBW) ($< 5\%$) and gain (~ 6 dBi) [1, 2]. Over the past several decades, a number of techniques for IBW and gain enhancement have been proposed, including the use of a thick, low ε_r dielectric substrate fed by an L-probe [3], multi-resonators in coplanar or stacked configurations [4, 5], resonant coupling aperture feed [6], slotted patches [7], and patch antennas operating in the higher-order modes [8–11]. These methods, however, have plenty of demerits, namely large size, increased height, and degraded radiation characteristics in terms of cross-polarization (xpol) [7], low front-to-back ratio (FBR) [6], as well as radiation pattern squint over the IBW [4].

On the other hand, applications such as multiple-input multiple-output (MIMO) antenna systems, reflector feed antennas, radar systems, and wide-angle scanning antenna array require compact, wideband, and high-gain attributes. To meet the aforesaid requirements, artificially engineered ground planes (GNDs) based on metamaterial (MTM) structure have been proposed as viable replacements for the traditional perfect electric conductor ground plane (PEC-GND). Moreover, due to its sub-wavelength scale, the two-dimensional (2D) version of the MTM, commonly known as high impedance surface (HIS), metasurface (MTS), artificial magnetic conductor (AMC), electromagnetic band gap (EBG), and reactive impedance surface (RIS), has received considerable interest of researchers working in the field of antennas [1, 2, 12–30, 34–42]. Although the AMC-based antennas operating at relatively low microwave frequency band in [1, 2, 12–30] have improved IBWs and moderate boresight gains, their

Received 9 March 2020, Accepted 10 June 2020, Scheduled 19 June 2020
* Corresponding author: Liguo Sun (liguos@ustc.edu.cn).
The authors are with the Electronic Engineering and Information Science, University of Science and Technology of China, China.

profiles and sizes are relatively large. Furthermore, composite right/left handed (CRLH) MTM-based antennas in [34, 35] have small sizes, extremely wide IBW, and an improved radiation efficiency, but they exhibit monopole-like radiation patterns, which may cause interference with neighboring wireless communication systems or unwanted reception and transmission of information to a particular direction. Besides being investigated for improving the IBW and gain of antennas, the 2D MTMs structures have been investigated for beam steering at millimeter wave band [36] and for the reduction of surface wave (SW) effects and dielectric substrate losses on chip antenna designs at THz band [37]. The 2D MTMs structures play a very critical role in reducing mutual coupling between closely spaced radiating elements in MIMO and radar antenna systems operating at both lower microwave frequency band [39, 40] and higher frequency band (THz) [41, 42].

This paper proposes a new way to enhance the IBW, boresight gain, FBR, and aperture efficiency of a linearly polarized rectangular LPRMPA mounted on a compact AMC-GND. The method uses large shorted unit cells at the center of the AMC and a wide slot cut on the AMC cells located underneath the patch to respectively depress the propagation of surface waves (SWs) and minimize the deleterious effect of the loading capacitance (C_{ov}) created between the AMC-GND and the radiating patch on the IBW. It is demonstrated that by suppressing (C_{ov}) and introducing a set of shorting pins, the antenna with dimensions of only $1\lambda_0 \times 0.6\lambda_0 \times 0.06\lambda_0$ can realize an IBW of 24%, a peak gain of 9.93 dBi, and a simulated aperture efficiency of greater than 96%. One of the many techniques for reducing the size of a patch antenna is by inserting an AMC surface with a high fringing capacitance between the patch radiator and its PEC-GND. It will be shown in this work, however, that this size reduction is realized at the cost of IBW, and the main objective of this paper is to enhance the IBW by eliminating the detrimental effect of the capacitive loading (Cov), while keeping the antenna size and volume as small as possible ($< \lambda_0$).

2. PROPOSED ANTENNA STRUCTURE AND OPERATIONAL MECHANISM

2.1. Antenna Structure and Evolution Process

A schematic diagram for the evolution process of the proposed compact, broadband probe-fed antenna, along with the optimized antenna dimensions, is shown in Figs. 1(a)–(d). As can be observed in Fig. 1(d), the antenna consists of two layers: the lower layer and the upper layer. The lower layer has a PEC-GND and an AMC surface on the bottom and top faces, respectively, as shown in Fig. 1(d), while an RMPA with dimensions of $L \times W$ is etched on the top face of the upper layer, as shown in

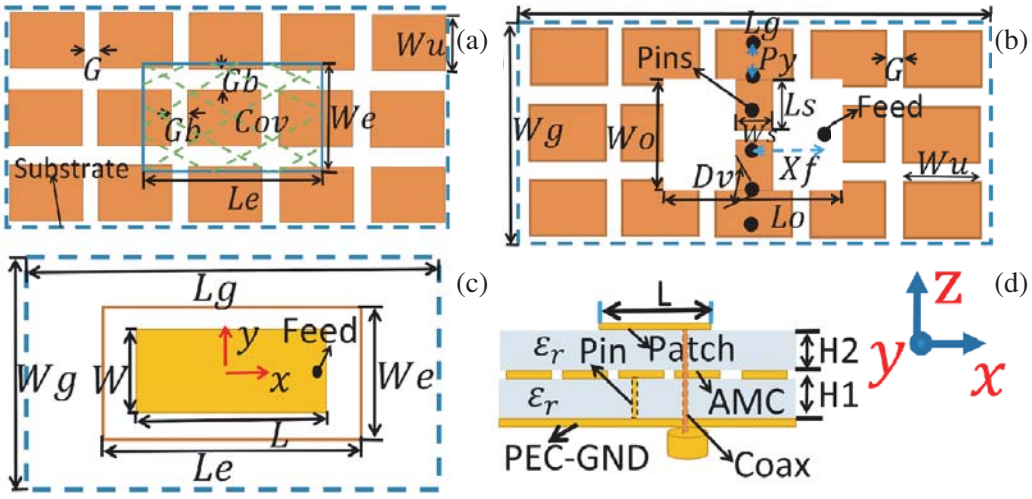

Figure 1. Proposed antenna structure (a) top view of the AMC showing the overlap area to be investigated, (b) optimized AMC surface with shorting pins, (c) top view of the rectangular patch with effective width (We) and length (Le), and (d) side view of the proposed antenna.

Figs. 1(c), (d). The two substrates have the same relative permittivity (ε_r) and height ($H1 = H2$). The AMC unit cells have a width (Wu), a spacing gap (G), and a periodicity of $p = Wu + G$, as seen in Fig. 1(a). An aperture with variable dimensions of $Le \times We$ and a variable gap (Gb) are introduced on the central unit cells located underneath the patch to demonstrate the effect of (Cov) that is created between the AMC-GND and the patch radiator on the resultant antenna IBW and resonant frequency (fr) [see Fig. 1(a)]. Moreover, as observed in Fig. 1(b), to simultaneously make the antenna symmetric and impede the propagation of SWs, two larger shorted unit cells are used at the center of the AMC. The shorting pins have a radius rv ($Dv = 2rv$) and a periodicity Py along the y-axis. The optimized antenna parameter dimensions are given in Table 1. It is instructive to mention that the length (L) and width (W) of the radiating RMPA are calculated using the cavity model based formulas available in [43], whereas the initial dimensions of the square unit cell are obtained using formulas in [44].

Table 1. Optimized antenna parameter dimensions.

Parameter	Wg	Lg	W	L	G	ε_r	Ws	Ls
Value (mm)	29.8	46.2	6.4	14.5	0.2	2.55	4.2	4.5
Parameter	Wo	Lo	$H1$	$H2$	Wu	Xf	Dv	n
Value (mm)	11.3	14.5	1.588	$H1$	8	3.6	0.6	6
Parameter	Py							
Value (mm)	2							

Unit is mm, except for ε_r and (n)

2.2. Operational Mechanism

From fundamental physics, it is well known that when two conductors are placed in parallel and close to each other at a distance $H2$, they form an overlay capacitor (Cov). The value of the capacitance depends on $H2$, dielectric constant ε_r, and overlap area A between the two conductors. This scenario describes well what happens when an AMC-GND is inserted between a PEC-GND and a radiating metal patch. The value of Cov can be calculated using Eq. (1) [31].

$$Cov = \frac{\varepsilon_0 \varepsilon_r A}{H2} = \frac{\varepsilon_0 \varepsilon_r LeWe}{H2} \tag{1}$$

where ε_r, ε_0, We, Le, and $H2$ are, respectively, the substrate relative permittivity, the free space permittivity, the effective width and length of the patch, and the thickness of the upper layer [see Fig. 1(d)]. Le is about $\lambda_g/2$ (λ_g is the guided wavelength in the substrate), while the value of We can be estimated using the well-known cavity model based formulas for the RMPA design [43]. Moreover, according to [13, 14], the AMC and the patch operating in a single separated mode can be modeled as simple $LiCi$ and $LpCpRp$ parallel resonant circuits, respectively. The inductance (Li) depends on the substrate thickness, while the fringing capacitance (Ci) depends on G, Wu, and the permittivity of the material surrounding the AMC. When an AMC surface is integrated with a conventional RMPA operating in a single separated mode, the equivalent circuit illustrated in Fig. 2(a) can be used to describe the resultant antenna resonant frequency response.

By excluding the feed probe inductance Xp, the resonant frequency (f_r) of Fig. 2(a) can be derived in three simple steps shown in Fig. 2(a) as 1, 2, and 3. The impedance (Z_1) of part 1 shown in blue is same as that of a parallel network given by Equation (2a), while the equivalent impedance of parts 1 and 2 ($Z_{1,2}$) is equal to that of the two capacitors connected in series, which gives an equivalent capacitor ($C1$), as can be seen in Equation (2b). The latter capacitor is now connected in parallel with the equivalent circuit of the patch shown in red giving Equation (2c). To deduce the resultant antenna resonant frequency (f_r), Equation (2c) is rearranged in a well-known form of a parallel RpC_TLp

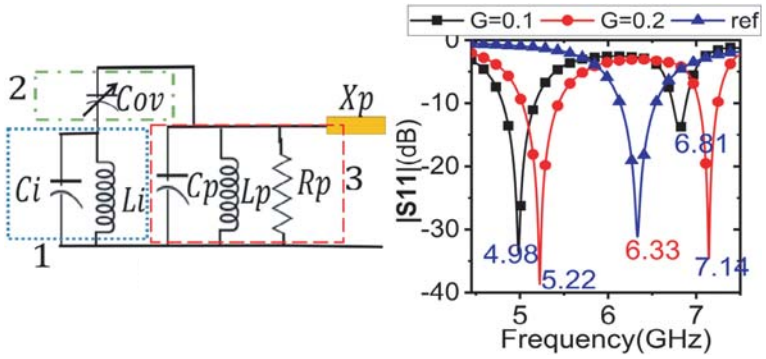

(a) (b)

Figure 2. (a) Proposed antenna simple equivalent circuit model; (b) simulated reflection coefficient for ant1 with gaps of 0.1 mm and 0.2 mm, and that of ref antenna.

resonant circuit, as can be found in Equation (2d)

$$Z_1 = \frac{\frac{1}{j\omega Ci} \times j\omega Li}{j\omega Li + \frac{1}{j\omega Ci}} = \frac{Li}{Ci}\frac{1}{j\omega\left(Li - \frac{1}{\omega^2 Ci}\right)} = \frac{Li}{Ci}\frac{1}{j\omega Ce} \tag{2a}$$

It is clear from Equation (2e) that f_r depends on Ci, Li, Cp, and Lp. More importantly, the total capacitance C_T increases with an increase in Cov when Xp, antenna size, and AMC size are fixed, which unfortunately decreases both the antenna f_r and IBW, since both these parameters are inversely proportional to the square root of C_T.

$$Z_{1,2} = \frac{Li}{Ci}\frac{1}{j\omega Ce} + \frac{1}{j\omega Cov} = \frac{1}{j\omega}\left(\frac{Li}{CiCe} + \frac{1}{Cov}\right) = \frac{1}{j\omega}\left(\frac{LiCov + CiCe}{CiCeCov}\right) \tag{2b}$$

$$Z_{1,2,3} = j\omega C1 + \frac{1}{Rp} + j\omega Cp + \frac{1}{j\omega Lp} = \frac{1}{Rp} + j\omega\left(\frac{CiCeCov}{LiCov + CiCe} + Cp\right) + \frac{1}{j\omega Lp} \tag{2c}$$

$$Z_{1,2,3} = j\omega C_T + \frac{1}{Rp} + \frac{1}{j\omega Lp} \tag{2d}$$

$$f_r = \frac{1}{2\pi\sqrt{C_T Lp}} \quad \text{where} \quad C_T = \frac{CiCeCov}{LiCov + CiCe} + Cp, \quad \text{and} \quad Ce = Li - 1/\omega^2 Ci \tag{2e}$$

Moreover, from Equation 2(e), one can see that when Cov is relatively small, f_r of the AMC loaded antenna is nearly the same as that of the antenna over a PEC-GND. Also, from Fig. 1(a) and Equation (1), it is evident that the value of Cov increases as $A = We \times Le$ increases (with smaller Gb), when $H2$ and ε_r are fixed. Note also that the fringing capacitance (Ci) and Cov are interrelated, that is, a small increase in Ci will lead to a considerable increase in Cov.

To validate the theoretical predictions above, a square unit cell is designed using formulas in [44], and numerical simulations are carried out in three ways: (1) increasing Ci by reducing G from 0.2 to 0.1 mm, while keeping other parameters fixed; (2) keeping $Gb = G$ fixed at 0.2 mm, while gradually varying We and Le; (3) leaving $Le = We = 0$ mm and $G = 0.2$ mm constant, while varying Gb. Figs. 3(a), (b) depict the simulated reflection phase and dispersion diagram of the square unit with and without the antenna substrate (cover), which in Figs. 3(a) and (b) is denoted as covered and uncovered, respectively. The covered and uncovered unit cells yield resonance (zero degree reflection phase frequency) and in-phase reflection (±90° BW) of 5.28 GHz and 19.09% (4.72–5.71 GHz), and 6.30 GHz and 20.37% (5.68–6.98 GHz), respectively. The downward shift in the AMC resonant frequency when the upper substrate is loaded is due to an increase in the effective capacitance [44]. Moreover, Fig. 3(b) illustrates that the propagation constant of the (TM) surface wave mode increases with the introduction of the top substrates. The increase in the propagation constant leads to the confinement of

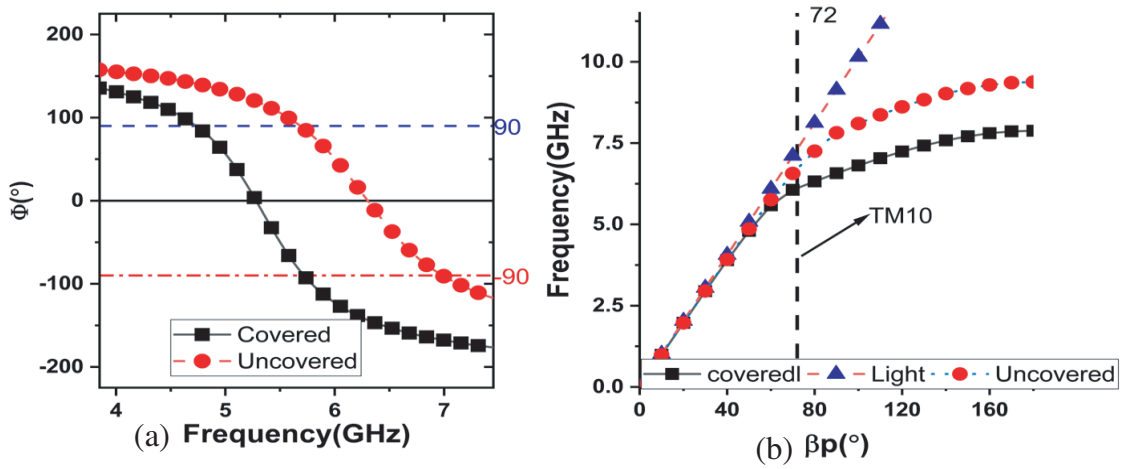

Figure 3. (a), (b) Simulated reflection phase and dispersion diagram of a square unit cell with $Wu = 8\,\text{mm}$ and $G = 0.2\,\text{mm}$ (ant1).

the E-fields within the substrate, which may degrade the antenna radiation patterns at the upper band edge. For example, the propagation constant at 6.7 GHz is 71.96° for the uncovered, which increases to about 95.80° with the loading of the top (antenna) substrate. The designed square unit cell is used to form an 5×3 AMC surface, and it serves as a ground plane for a conventional RMPA. Figs. 2(b), 4(a)–(c), and 4(d) show the simulated results for the previously mentioned three cases. For comparison, antennas etched on a traditional PEC-GND and that on an AMC-GND with $Wu = 8\,\text{mm}$ $G = 0.2$ mm are simulated as well andk referred to as ref and ant1, respectively.

As seen in Fig. 2(b), ref has a resonant frequency of 6.33 GHz, while ant1 resonates at 5.22 and 7.14 GHz, respectively. When G is reduced to 0.1 mm, the resonance frequencies of ant1 decrease to 4.98 and 6.81 GHz, respectively. The resonance frequency of ref is reduced from 6.33 GHz to 4.98 GHz with the integration of the AMC surface of $G = 0.1\,\text{mm}$. This reduction in ant1 resonance frequencies is due to the slight increase in (Ci), which in turn significantly increases Cov and C_T, as illustrated in Fig. 1(a), and Equations (1) and (2e). Fig. 3(b) depicts the simulated dispersion diagram for a square unit cell with $Wu = 8\,\text{mm}$, $G = 0.2\,\text{mm}$ and the vertical line representing Equation (3) [23, 38]. Ant1 realizes a resonant frequency of 6.86 GHz in the higher frequency region, which is very close to 7.14 GHz in Fig. 2(b). Therefore, the higher resonant frequency for ant1, hereafter denoted as (frs), is due to the SWs propagating on the AMC. In Equation (3), $\beta_{sw(x,y)}$, $P_{(x,y)}$, and $N_{(x,y)}$ represent, respectively, the surface wave propagation constant, unit cell periodicity, and the number of cells along the x and y. Note that in Fig. 3(b), m is taken to be 2, since it lies within the slow wave region of the dispersion diagram, whereas $N_{(x,y)} = N_{(x)} = 5$ is used [see Fig. 6(d)]. Note that for both $G = 0.1\,\text{mm}$ and $G = 0.2\,\text{mm}$ cases, the ratio frs/fr is around 1.37, resulting in a dual-band operation, rather than a broadband one, as clearly seen in Fig. 2(b).

$$\beta_{sw(x,y)} = \frac{m\pi}{P_{(x,y)}N_{(x,y)}}, \quad m = 1, 2, 3, \ldots, \tag{3}$$

To enlarge the IBW of ant1, while at the same time compensate the decrease in the resonance frequency of ref, the impact of Cov on the resonant frequency response of ant1 is studied by gradually reducing Cov, as shown in Figs. 4(a)–(d). From Fig. 4(a), it is clear that the input impedance (Zin) of ant1 is highly capacitive, and it becomes inductive as Cov gets higher. The increase in Cov (large removed area) leads to an increase in the resonant frequency of ant1, as shown in Figs. 4(b)–(d), thereby compensating the decrease in ref resonance without any modification on either patch or other exterior AMC cells. For example, for a non-optimized Xp, when Cov is 0.65, 1.68, and 2.36 pF, f_r of ant1 varies to 5.37, 5.8, and 6.2 GHz, respectively, as observed in Fig. 4(b). Moreover, with an optimized Xp, Cov of 1.8 pF yields a fr of nearly the same as that of ref, as illustrated in Fig. 4(c). For $Cov = 1.94\,\text{pF}$, which corresponds to a total cut area of $Wo(We) \times Lo(Le) = 11.3\,\text{mm} \times 12.1\,\text{mm}$), ant1 realizes an IBW of 24.7% (5.5–7.05 GHz) with two reflection zeros in the $|S11| < -10\,dB$ curve, as seen in Fig. 4(c).

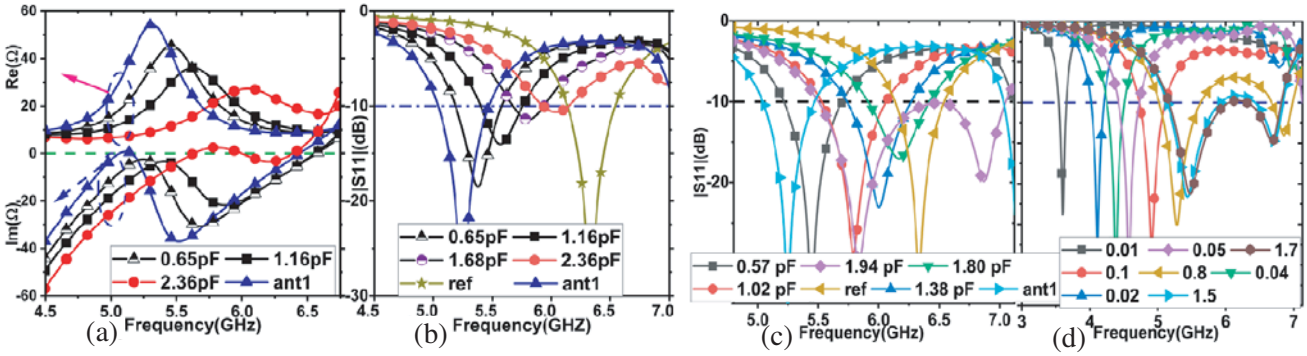

Figure 4. Effect of Cov on ant1 resonance behavior: (a), (b) input impedance and reflection coefficient as a function of $WeLe$, when the feed probe is fixed (Xp not optimized); (c), (d) the impact of varying $WeLe$ and Gb(in mm) on ant1 IBW with optimized feed position (Xp is optimized); respectively.

This IBW is about three times of those of ant1 on an AMC without an aperture and [12], while all the antenna configurations have the same dimensions and are printed on the same dielectric materials. This wider IBW is due to the merge of f_r and f_{rs}, since the ratio frs/fr decreases with increasing Cov, as shown in Fig. 4(b) for $Cov = 2.36$ pF; however, for all the results shown in Fig. 4, the change in frs as a function of Cov is not plotted for reason of clarity.

The detrimental effect of Cov on ant1 IBW and resonance is further demonstrate by gradually reducing Gb while keeping Wu and G fixed at 8 mm and 0.2 mm. For Gb of 0.01, 0.03, and 0.05 mm, ant1 f_r and IBW vary, respectively, to 3.6 GHz and 3% (3.54–3.65 GHz), 4.38 GHz and 5.9% (4.25–4.5 GHz), and 4.57 GHz and 6.7% (4.42–4.72 GHz), conforming the expressions (1) and (2e). Furthermore, with $Gb = 1.7$ mm, ant1 IBW is raised to 27.75% (5.15–6.81 GHz), i.e., IBW enhancement of more than three times is obtained as compared to ref, ant1 (without an aperture) and [12]. An IBW improvement of 3% is achieved compared to ant1 with $Cov = 1.94$ pF, which can be attributed to the additional inductance introduced by the refilled area. This antenna configuration is hereafter labeled ant2, and according to simulations, with this configuration, antennas on AMC surface with 3×2 ($0.53\lambda_0 \times 0.36\lambda_0 \times 0.06\lambda_0$) and $3 \times 3(0.53\lambda_0 \times 0.53\lambda_0 \times 0.06\lambda_0)$ unit cells can easily obtain IBWs and peak gains of 17.1% and 6.2 dBi, and 20.7% and 7 dBi, respectively.

The influence of Ws and Ls, which are introduced in ant1 with a removed area of $Wo{\times}Lo$ ($Cov = 1.94$ pF) to restore the antenna symmetry and improve the FBR, while still reducing the deleterious effect of Cov on ant1 IBW and f_r is shown in Figs. 5(a), (b). As observed, with the

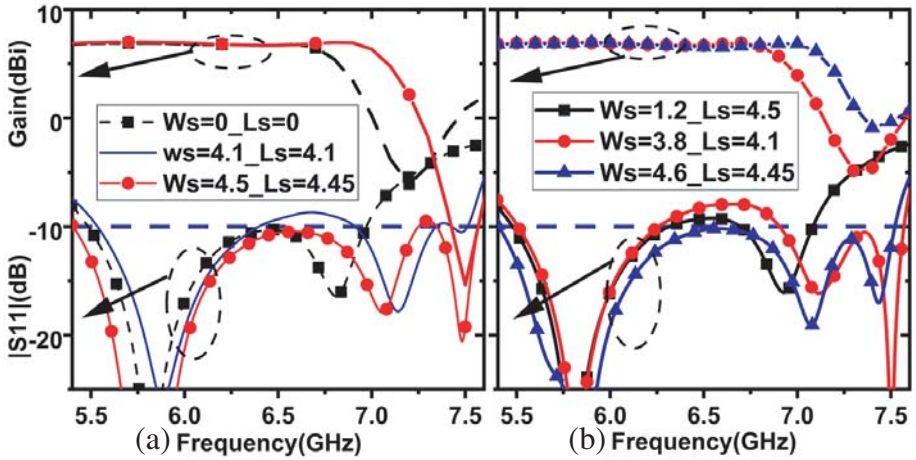

Figure 5. Effects of Ws, Ls on the IBW and boresight gain of ant1 with a removed area of $Wo \times Lo$.

introduction of Ws and Ls, a new resonance emerges at 7.4 GHz, and the boresight gain BW improves slightly at the upper band edge as compared to ($Ws = Ls = 0$ mm) due to an increase in FBR. By varying Ws and Ls from 0–0 mm to 3.8–4.1 mm, the antenna $|S11|$ curve yields, respectively, two and three reflection zeros, as illustrated in Figs. 5(a), (b). With $Ws = Ls = 4.1$ mm, ant1 impedance matching improves slightly. Better impedance matching and larger IBW of 33.6% (5.4–7.57 GHz) are obtained with $Ws = 4.4$–4.6 mm and $Ls = 4.45$ mm, while the antenna overall size remains only $0.89\lambda_0 \times 0.53\lambda_0 \times 0.06\lambda_0$ ($< \lambda_0$). Moreover, since the antenna total efficiency (Te) is determined in part by the mismatch efficiency (reflection efficiency), it can be deduced from Figs. 5(a), (b) that the integration of Ws and Ls onto the AMC-GND has improved the antenna (Te) at the upper band edge.

Although the introduction of Ws and Ls onto the AMC has slightly improved the antenna FBR and IBW, the peak gain remains constant at 6.8 dBi. The lower gain can be attributed to the diffraction of SWs at the edge of the substrate and the out-of-phase current distribution on the AMC, as illustrated in Figs. 6(a), (b). On the other hand, it is well known that in TM SWs, the surface currents are parallel to the surface, and therefore, a wall of shorting pins can be used to prevent them from reaching the substrate edge. Moreover, shorted unit cell can be considered a composite right/left-handed (CRLH) transmission line whereby the phase advance of the LH cancels the phase lag of the RH, resulting in an in-phase surface current distribution shown in Fig. 6(d) [32].

Figure 7 depicts the effect of the shorting pins on the IBW and gain. For $n = 7$, 11 and $Xf = 1.6$ mm, the IBW shifts from 5.17–6.99 to 4.95–6.94 GHz. In contrast, with $Xf = -1.5$ mm and $n = 11$, the IBW moves rightward (5.58–7.19 GHz). The lower and upper shifts in IBW are due

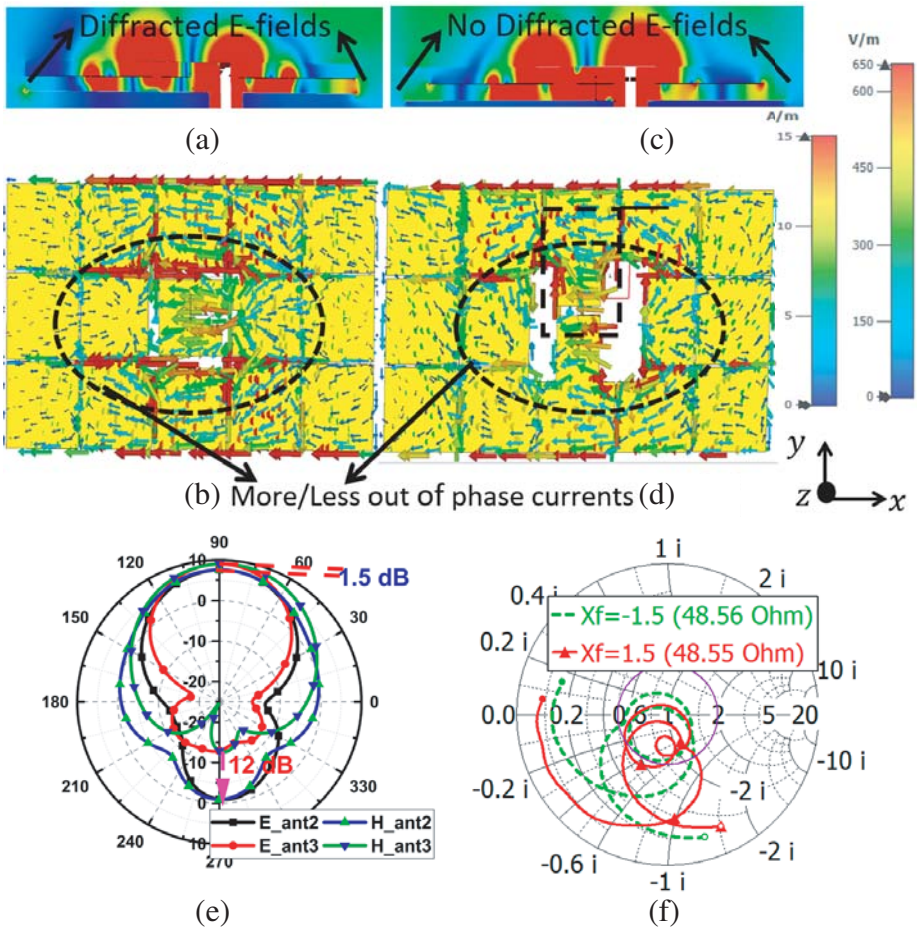

Figure 6. (a), (b) Simulated E-field surface, (c), (d) current at 7 GHz of ant2 and proposed (ant3), respectively, (e) Comparison of the simulated co-polarization (copol) pattern at 7 GHz, (f) Smith chart illustrating how ant input impedance changes as a function of Xf.

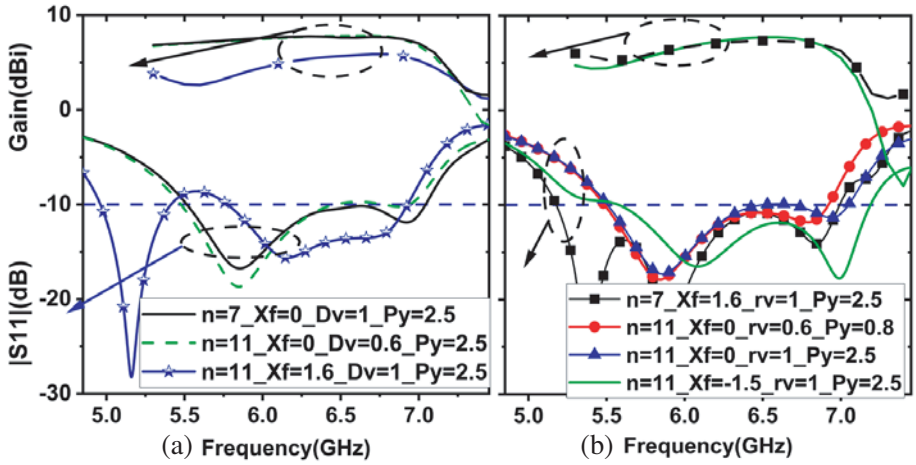

Figure 7. Effect of the shorting pins loaded on the central large cells on the ant1boresight gain and IBW.

to the capacitive and inductive coupling that is created when the pins are close to or away from the feed probe, respectively, as seen in Fig. 6(f). With n= 11, Py = 2.5 mm, and Xf = 0 mm, varying Dv from 0.6 to 1 mm shifts the IBW from 5.47–6.96 GHz to 5.5–7.05 GHz due to a decrease in the effective permittivity (ε_{eff}), as large holes are drilled in the substrate. When Py is varied from 0.8 to 2.5 mm, while keeping n = 11, Xf = 0 mm and Dv = 0.6 mm fixed, the IBW and gain remain constant. In the above cases, Xf and n significantly affect both the antenna IBW and gain, while Dv and Py exhibit little effect on them, mainly because the coupling heavily depends on (n). Better radiation characteristics are obtained with Xf= 0 and n= 6, and the antenna FBR and gain are respectively improved by more than 12 dB and 1.5 dB in both the E and H planes at 7 GHz, as seen in Fig. 6(e). Ant1 with and without pins has a peak gain of 7.6 dBi at 6.9 GHz and 9.5 dBi at 7.4 GHz, respectively. Ant1 with optimized two large central shorted cells and wide slot is hereafter referred to as ant3. Using $Ae = 100 \times Gain\lambda_0^2/(4\pi A)$ [33], ant3 obtains a simulated aperture efficiency varying between 96 and 120% over the frequency band of 5.3–7.3 GHz. Thus, the proposed technique can improve the antenna FBR and efficiency with a simple configuration, unlike classical cavity backed patch antennas, which require at least $0.2\lambda_0$ separation distance between the cavity walls and patch edges.

3. EXPERIMENTAL RESULTS

Figures 8(a) and (b) display the simulated (sim) and measured (mes) $|S11| < -10\,dB$ IBWs of ant1, ant2, and ant3, while Fig. 8(c) depicts the simulated and measured gains of ant3 with and without the air gap. Note that for comparison, Fig. 8(c) includes also the simulated gain of ant2. Ant1, ant2, and ant3 realize IBWs of 8.5% (4.96–5.40 GHz), 27.30% (5.63–7.45 GHz), and 24% (6.07–7.73 GHz), respectively. The measured results of ant2 and ant3 are shifted rightward due to the small air gap that might have been introduced between the lower and upper substrates during the antenna assembly, as shown in Fig. 8(b) for an air gap of 0.1 mm. Note also that both ant2 and ant3 exhibit two dips in their $|S11|$ curves, one at 6.1 and the other at 7.1 GHz, which are the TM10 modes of the patch (fr) and SWs (frs), as seen in Figs. 2(b), 3(b), 4(b)–(d), and 6(d). Moreover, Figs. 9(a) and (b) show the simulated and measured E and H-planes copolar (copol) and cross-polarization (xpol) radiation patterns at 6.4 GHz of ant3, whereas Figs. 9(c) and (d) show photos of the fabricated prototypes of ant1, ant2, and ant3. The measured Xpol level is 18 dB below the copol level, while the FBRs are greater than 17 dB. The simulated 3-dB beamwidths in E and H planes are 58.8° and 79.5°, respectively. Over the IBW, ant3 has simulated and measured peak gains of 9.45 dBi at 7.4 GHz and 9.93 dBi at 7.3 dBi. The higher measured gain than the simulated one can be attributed to the air gap that might have been created between the two substrates during the antenna measurement. In addition, the accuracy in measuring the antenna gain decreases as its size becomes smaller.

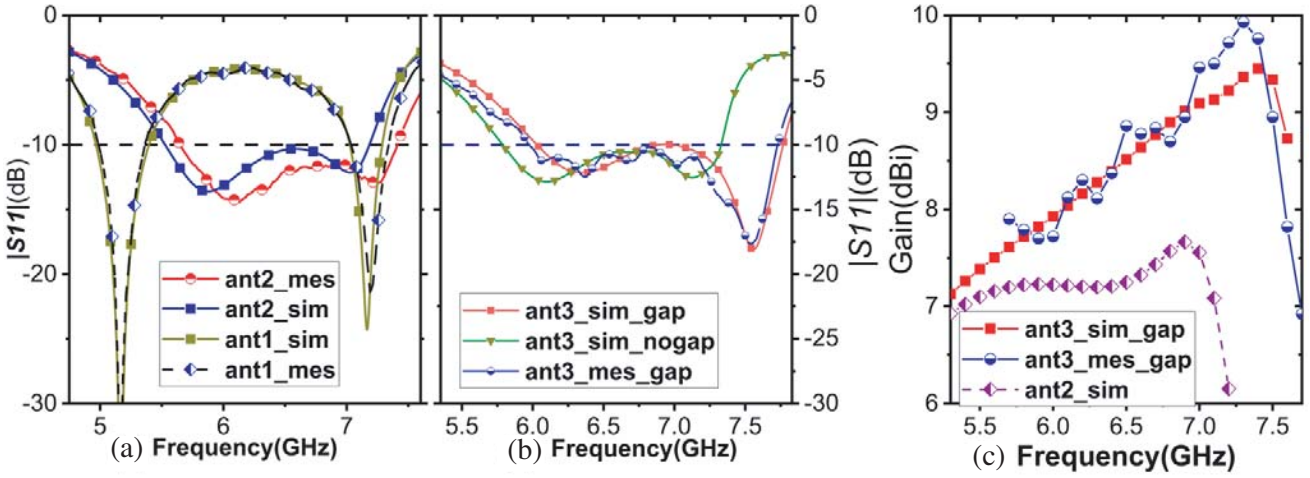

Figure 8. (a) Simulated (sim) and measured (mes) $|S11| < -10$ dB IBW of ant1 and ant2; (b) simulated $|S11|$ of ant3 with and without the air gap (0.1 mm), and (c) simulated, measured gains of ant3 and ant2 (sim only), respectively.

As seen in Table 2, in comparison to the recently reported AMC-backed MPAs, the proposed antennas have attractive features of wider IBW, compact size ($\leq\lambda_0$), and low profile. Moreover, ant3 obtains improved FBR, stable boresight gain, and higher aperture efficiency over its IBW.

Table 2. Comparison of the proposed antenna with reference.

Ref.	Size	Peak gain (dBi)	and Ae(%)	(IBW %)
[1]	$1.39\lambda_0 \times 1.39\lambda_0 \times 0.07\lambda_0$	9.77	40.24	13.66
[9]	$1.65\lambda_0 \times 1.65\lambda_0 \times 0.04\lambda_0$	11.5	33.61	3
[11]	$2.83\lambda_0 \times 2.83\lambda_0 \times 0.08\lambda_0$	11.84	11.76	17.6
[13]	$1.1\lambda_0 \times 1.1\lambda_0 \times 0.06\lambda_0$	10.3	67.74	21
[15]	$1\lambda_0 \times 1\lambda_0 \times 0.06\lambda_0$	11.7	93.10	10.5
[16]	$0.87\lambda_0 \times 0.87\lambda_0 \times 0.19\lambda_0$	7	73.59	31
[17]	$0.66\lambda_0 \times 0.94\lambda_0 \times 0.05\lambda_0$	9.36	120.05	11.7
[18]	$1\lambda_0 \times 1\lambda_0 \times 0.05\lambda_0$	12.8	101.85	16.4
[19]	$1.78\lambda_0 \times 1.78\lambda_0 \times 0.07\lambda_0$	10.3	25.87	29.0
[20]	$1.55\lambda_0 \times 1.55\lambda_0 \times 0.11\lambda_0$	12.5	41.40	24.3
[21]	$1.3\lambda_0 \times 1.3\lambda_0 \times 0.05\lambda_0$	12.48	56.14	18.2
[25]	$1.9\lambda_0 \times 0.7\lambda_0 \times 0.15\lambda_0$	9.2	55.04	32.6
[27]	$1.09\lambda_0 \times 1.09\lambda_0 \times 0.07\lambda_0$	10.9	73.00	18.1
[28]	$1.35\lambda_0 \times 1.35\lambda_0 \times 0.051\lambda_0$	10.5	45.84	13
[29]	$1.17\lambda_0 \times 0.99\lambda_0 \times 0.07\lambda_0$	9.3	63.89	26
Ant 2.	$0.89\lambda_0 \times 0.53\lambda_0 \times 0.06\lambda_0$	7	118.09	27.3
Ant 3.	$1\lambda_0 \times 0.6\lambda_0 \times 0.06\lambda_0$	9.93	131.70	24

All the antennas in the table are AMC-based except for [9, 11], which are high order mode patches. The calculation of the aperture efficiency takes the size of the GND into account, not just the radiating element aperture.

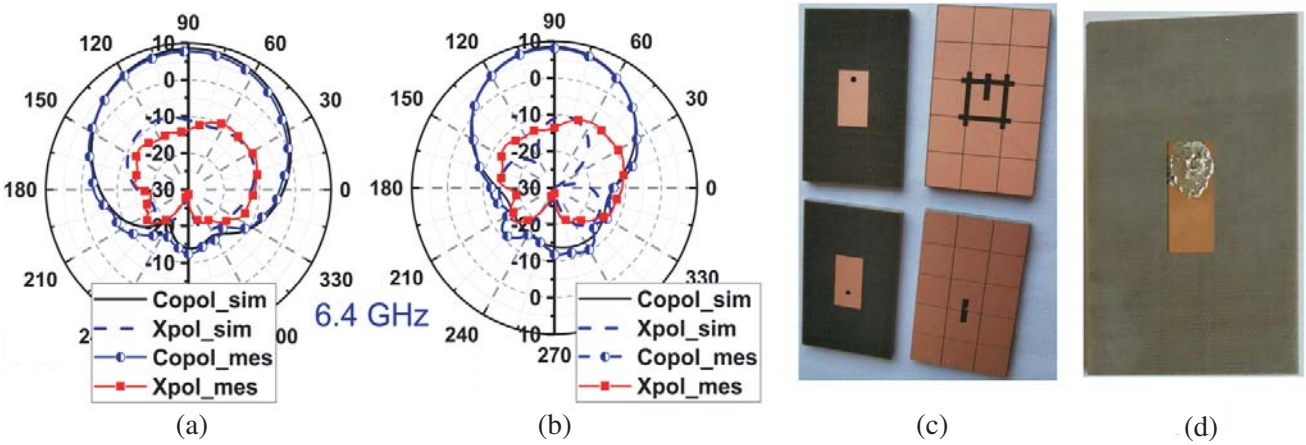

Figure 9. (a), (b) Simulated (sim) and measured (mes) copol and xpol H and E-planes at 6.4 GHz, respectively, whereas (c), (d) are the fabricated photos of ant1, ant2 and ant3, respectively.

4. CONCLUSION

This work presents a compact, low profile AMC-backed RMPA with improved impedance and radiation characteristics. The broader IBW ($> 24\%$) and gain of more than 9.5 dBi are obtained due respectively to the suppression of the deleterious effect of the loading capacitance on the IBW and use of the shorting pins to impede the propagation surface waves. Moreover, the proposed antenna realizes a simulated aperture efficiency higher than (96%), measured boresight peak gain (9.93 dBi), and FBR of greater than 15 dB, while maintaining an overall size of only $1\lambda_0 \times 0.6\lambda_0 \times 0.06\lambda_0$. For its compactness, good radiation, and impedance performances, the presented antenna can be used in various applications, such as MIMO antenna system, wide-angle scanning antenna array, and reflector feed antennas operating in satellite C-band 5.9–6.4 GHz and 6.425–6.75 GHz.

REFERENCES

1. Qu, D., L. Shafai, et al., "Improving microstrip patch antenna performance using EBG substrates," *IEE Proceedings — Microwaves, Antennas Propag.*, Vol. 153, No. 6, 558–563, Dec. 2006.
2. Ntawangaheza, J. D., L. Sun, et al., "Thin profile wideband and high gain microstrip patch antenna on a modified AMC," *IEEE Antennas Wireless Propag. Lett.*, Vol. 18, No. 12, 2518–2522, Dec. 2019.
3. Luk, K. M., C. L. Mak, et al., "Broadband microstirp patch antenna," *Electron. Let.*, Vol. 34, 1442–1443, 1998.
4. Aanandan, C. K., P. Mohanan, et al., "Broad-band gap coupled microstrip antenna," *IEEE Trans. Antennas Propag.*, Vol. 38, No. 10, 1581–1586, Oct. 1990.
5. Lee, R. Q. and K. Lee, "Experimental study of the two-layer electromagnetically coupled rectangular patch antenna," *IEEE Trans. Antennas Propag.*, Vol. 38, No. 8, 1298–1302, Aug. 1990.
6. Targonski, S. D., R. B. Waterhouse, et al., "Design of wide-band aperture stacked microstrip patch antennas," *IEEE Trans. Antennas Propag.*, Vol. 46, No. 9, 1245–1251, 1998.
7. Clenet, M. and L. Shafai, "Multiple resonances and polarisation of U-slot patch antenna," *Electron. Lett.*, Vol. 35, No. 2, 101–103, Jan. 21, 1999.
8. Khan, Q. U., D. Fazal, et al., "Use of slots to improve performance of patch in terms of gain and sidelobes reduction," *IEEE Antennas Wireless Propag. Lett.*, Vol. 14, 422–425, 2015.
9. He, Y., Y. Li, et al., "Dual linearly polarized microstrip antenna using a slot-loaded TM_{50} mode," *IEEE Antennas Wireless Propag. Lett.*, Vol. 17, No. 12, 2344–2348, Dec. 2018.

10. Zhang, X. and L. Zhu, "Gain-enhanced patch antennas with loading of shorting pins," *IEEE Trans. Antennas Propag.*, Vol. 64, No. 8, 3310–3318, Aug. 2016.
11. Umar Khan, Q., M. Bin Ihsan, et al., "Higher order modes: A solution for high gain, wide band patch antennas for different vehicular applications," *IEEE Trans. Vehicular Technology*, Vol. 66, No. 5, 3548–3554, May 2017.
12. Foroozesh, A. and L. Shafai, "Improvements in the performance of compact microstrip antennas using AMC ground planes," *2010 14th International Symposium on Antenna Technology and Applied Electromagnetics & the American Electromagnetics Conference*, 1–4, Ottawa, ON, 2010.
13. Majumder, B., K. Krishnamoorthy, et al., "Compact broadband directive slot antenna loaded with cavities and single and double layers of metasurfaces," *IEEE Trans. Antennas Propag.*, Vol. 64, No. 11, 4595–4606, Nov. 2016.
14. Malekpoor, H. and S. Jam, "Improved radiation performance of low profile printed slot antenna using wideband planar AMC surface," *IEEE Trans. Antennas Propag.*, Vol. 64, No. 11, 4626–4638, Nov. 2016.
15. Chen, D., W. Yang, and W. Che, "High-gain patch antenna based on cylindrically projected EBG planes," *IEEE Antennas Wireless Propag. Letts.*, Vol. 17, No. 12, 2374–2378, Dec. 2018.
16. Zhu, S. Li, et al., "Wideband low-profile highly isolated MIMO antenna with artificial magnetic conductor," *IEEE Antennas Wireless Propag. Letts.*, Vol. 17, No. 3, 458–462, Mar. 2018.
17. Yang, W., H. Wang, et al., "A wideband and high-gain edge-fed patch antenna and array using artificial magnetic conductor structures," *IEEE Antennas Wireless Propag. Lett.*, Vol. 12, 769–772, 2013.
18. Yang, W., D. Chen, et al., "High-efficiency high-isolation dual-orthogonally polarized patch antennas using nonperiodic RAMC structure," *IEEE Trans. Antennas Propag.*, Vol. 65, No. 2, 887–892, Feb. 2017.
19. Foroozesh, A. and L. Shafai, "Application of combined electric- and magnetic-conductor ground planes for antenna performance enhancement," *Canadian Journal of Electrical and Computer Engineering*, Vol. 33, No. 2, 87–98, Spring 2008.
20. Jagtap, S., A. Chaudhari, N. Chaskar, et al., "A wideband microstrip array design using RIS and PRS layers," *IEEE Antennas Wireless Propag. Letters*, Vol. 17, No. 3, 509–512, Mar. 2018.
21. Yang, W., W. Che, and H. Wang, "High-gain design of a patch antenna using stub-loaded artificial magnetic conductor," *IEEE Antennas Wireless Propag. Letters*, Vol. 12, 1172–1175, 2013.
22. Liu, W., Z. N. Chen, et al., "Metamaterial-based low-profile broadband aperture-coupled grid-slotted patch antenna," *IEEE Trans. Antennas Propag.*, Vol. 63, No. 7, 3325–3329, Jul. 2015.
23. Liu, W., Z. N. Chen, and X. Qing, "Metamaterial-based low-profile broadband mushroom antenna," *IEEE Trans. Antennas Propag.*, Vol. 62, No. 3, 1165–1172, Mar. 2014.
24. Gao, G., C. Yang, B. Hu, R. Zhang, and S. Wang, "A wearable PIFA with an all-textile metasurface for 5 GHz WBAN applications," *IEEE Antennas Wireless Propag. Lett.*, Vol. 18, No. 2, 288–292, Feb. 2019.
25. Mateos, R. M., C. Craeye, and G. Toso, "High-gain wideband low-profile anenna," *Microw. Opt. Techol. Lett.*, Vol. 48, No. 12, 2615–2619, 2006.
26. Zhong, Y., G. Yang, et al., "Gain enhancement of bow-tie antenna using fractal wideband artificial magnetic conductor ground," *Electron. Lett.*, Vol. 51, No. 4, 315–317, 2015.
27. Nie, N., X. Yang, Z. N. Chen, and B. Wang, "A low-profile wideband hybrid metasurface antenna array for 5G and WiFi systems," *IEEE Trans. Antennas Propag.*, Vol. 68, No. 2, 665–671, Feb. 2020.
28. Alharbi, M., C. A. Balanis, et al., "Hybrid circular ground planes for high-realized-gain low-profile loop antennas," *IEEE Antennas Wireless Propag. Lett.*, Vol. 17, No. 8, 1426–1429, Aug. 2018.
29. Sun, W., Y. Li, Z. Zhang, and P. Chen, "Low-profile and wideband microstrip antenna using quasi-periodic aperture and slot-to-CPW transition," *IEEE Trans. Antennas Propag.*, Vol. 67, No. 1, 632–637, Jan. 2019.
30. Li, T. and Z. N. Chen, "A dual-band metasurface antenna using characteristic mode analysis," *IEEE Trans. Antennas Propag.*, Vol. 66, No. 10, 5620–5624, Oct. 2018.

31. Yang, M., Z. N. Chen, P. Y. Lau, X. Qing, and X. Yin, "Miniaturized patch antenna with grounded strips," *IEEE Trans. Antennas Propag.*, Vol. 63, No. 2, 843–848, Feb. 2015.
32. https://en.wikipedia.org/wiki/Metamaterial_antenna (accessed 29 Nov. 2019).
33. Canet-Ferrer, J., "Metamaterials and metasurfaces," *Intechopen*, 2019.
34. Alibakhshikenari, M., Virdee, et al., "Extended aperture miniature antenna based on CRLH metamaterials for wireless communication systems operating over UHF to C-band," *Radio Science*, Vol. 53, No. 2, 154–165, Feb. 2018.
35. Alibakhshikenari, M., B. S. Virdee, et al., "Miniaturized planar-patch antenna based on metamaterial L-shaped unit-cells for broadband portable microwave devices and multiband wireless communication systems," *IET Microwaves, Antennas & Propagation*, Vol. 12, No. 7, 1080–1086. Jun. 2018.
36. Alibakhshikenari, M., et al., "Beam-scanning leaky-wave antenna based on CRLH-metamaterial for millimeter-wave applications," *IET Microwaves, Antennas & Propagation*, Vol. 13, No. 8, 1129–1133, Jul. 2019.
37. Alibakhshikenari, M., B. S. Virdee, C. H. See, et al., "High-gain metasurface in polyimide on-chip antenna based on CRLH-TL for sub terahertz integrated circuits," *Sci. Rep.*, Vol. 10, 4298, Mar. 2020.
38. Alharbi, M. S., C. A. Balanis, et al., "Performance enhancement of square-ring antennas exploiting surface-wave metasurfaces," *IEEE Antennas Wireless Propag. Lett.*, Vol. 18, No. 10, 1991–1995, Oct. 2019.
39. Alibakhshikenari, M., et al., "Isolation enhancement of densely packed array antennas with periodic MTM-photonic bandgap for SAR and MIMO systems," *IET Microwaves, Antennas & Propagation*, Vol. 14, No. 3, 183–188, Feb. 2020.
40. Alibakhshikenari, M., M. Khalily, B. S. Virdee, et al., "Mutual coupling suppression between two closely placed microstrip patches using EM-bandgap metamaterial fractal loading," *IEEE Access*, Vol. 7, 23606–23614, Mar. 5, 2019.
41. Alibakhshikenari, M., B. S. Virdee, et al., "Study on isolation and radiation behaviours of a 34×34 array-antennas based on SIW and metasurface properties for applications in terahertz band over 125–300 GHz," *Optik, International Journal for Light and Electron Optics*, Dec. 2019.
42. Alibakhshikenari, M., B. S. Virdee, et al., "Meta-surface wall suppression of mutual coupling between microstrip patch antenna arrays for THz-band applications," *Progress In Electromagnetics Research Letters*, Vol. 75, 105–111, 2018.
43. Wang, Z., et al., "An accurate edge extension formula for calculating resonant frequency of electrically thin and thick rectangular patch antennas," *IEEE Access*, Vol. 4, 2388–2397, Jun. 2016.
44. Sievenpiper, D., L. Zhang, et al., "High-impedance electromagnetic surfaces with a forbidden frequency band," *IEEE Trans. Micr. Theory Tech.*, Vol. 47, No. 11, 2059–2074, Nov. 1999.